Drivers of Future Extratropical Sea Surface Temperature Variability Changes in the North Pacific

Jacob Gunnarson (jlgunnar@hawaii.edu)
University of Hawai i at Mānoa https://orcid.org/0000-0001-9915-4330
Malte Stuecker
University of Hawaii at Manoa https://orcid.org/0000-0001-8355-0662
Sen Zhao
University of Hawaii at Manoa https://orcid.org/0000-0002-5597-1109

Article

Keywords:

Posted Date: February 14th, 2024

DOI: https://doi.org/10.21203/rs.3.rs-3935510/v1

Additional Declarations: (Not answered)

Drivers of Future Extratropical Sea Surface Temperature Variability Changes in the North Pacific

Jacob L. Gunnarson[1*], Malte F. Stuecker[1,2] and Sen Zhao[3]

[1*]Department of Oceanography, University of Hawai'i at Mānoa, 1000 Pope Road, Honolulu, 96822, HI, USA.
[2]International Pacific Research Center, University of Hawai'i at Mānoa, 1680 East-West Road, Honolulu, 96822, HI, USA.
[3]Department of Atmospheric Sciences, University of Hawai'i at Mānoa, 2525 Correa Road, Honolulu, 96822, HI, USA.

*Corresponding author(s). E-mail(s): jlgunnar@hawaii.edu;
Contributing authors: stuecker@hawaii.edu; zhaos@hawaii.edu;

Abstract

Under anthropogenic warming, future changes to climate variability beyond specific modes such as the El Niño-Southern Oscillation (ENSO) have not been well-characterized. In the Community Earth System Model version 2 Large Ensemble (CESM2-LE) climate model, the future change to sea surface temperature (SST) variability (and correspondingly marine heatwave intensity) is spatially heterogeneous. We examined these projected changes (between 1960-2000 and 2060-2100) in the North Pacific using a local linear stochastic-deterministic model, which allowed us to quantify the effect of changes to three drivers on SST variability: ocean "memory" (the SST damping timescale), ENSO teleconnections, and stochastic noise forcing. The ocean memory declines in most areas, but lengthens in the central North Pacific. This change is primarily due to changes in air-sea feedbacks and ocean damping, with the shallowing mixed layer depth playing a secondary role. An eastward shift of the ENSO teleconnection pattern is primarily responsible for the pattern of SST variance change.

1 Introduction

Anthropogenic emissions of greenhouse gasses are causing profound changes to the Earth's climate. Changes to the climate mean state have been studied for over half a century (e.g., ref. [1]) and are often used to set targets for reducing greenhouse gas emissions. In contrast, changes to climate variability—characterized statistically by variance and occurrence of extreme events and of importance for regional adaptation strategies—under future warming scenarios are less well understood.

There is a substantial body of literature characterizing future changes to specific modes of climate variability such as the El Niño-Southern Oscillation (ENSO) [2–8] and the Madden-Julian Oscillation [9–12]. However the broader study of climate variability changes is an emerging field with many outstanding questions [13–15].

The recent advent of large ensemble climate model simulations offers an opportunity to robustly quantify future variance and extreme event changes [13, 16–18]. Conducting a large number of simulations with the same climate model with identical external forcing but perturbed initial conditions allows for a clear identification of the forced signal as it changes over time, leaving only model and scenario uncertainty [19].

In this study, we examined the projected change to sea surface temperature (SST) variability in the North Pacific and its physical drivers using the Community Earth System Model version 2 Large Ensemble (CESM2-LE), which consists of 100 ensemble member simulations [13]. Changes to SST variability are of key importance to both physical and biological components of the climate system: SSTs couple the ocean and atmosphere via radiative and turbulent heat fluxes [20] and control many physiological processes of marine organisms [21]. The occurrence of marine heatwaves, prolonged periods of anomalously high SST that result in severe ecological and socioeconomic impacts [22], is directly related to SST variability from a moving baseline perspective [23, 24].

Strikingly, the projected change in SST variance in CESM2-LE between 1960-2000 and 2060-2100 is not spatially uniform (Fig. 1c, d), and the aim of this study was to identify the drivers responsible for this pattern of variability change. Note that these projected changes in variance directly translate (if the other statistical moments remain constant) to changes of threshold exceedances of upper percentiles (e.g., the 90^{th} percentile) that are often used to define marine heatwaves (e.g., ref. [25]). The area-weighted spatial pattern correlation coefficient between the SST standard deviation change (Fig. 1e) and marine heatwave intensity change (Fig. 1f) globally is 0.87.

We used a local linear stochastic SST model to quantify the relative effect of changes to three drivers on the overall change in SST variance: ocean memory, ENSO teleconnections, and stochastic noise forcing.

2 Methods

2.1 Data

We used the Community Earth System Model version 2 Large Ensemble in this study. CESM2 is a coupled Earth system model with active ocean biogeochemistry [26]. The model incorporates the CAM6 atmosphere model and POP2 ocean model, both on $\sim 1^\circ$ horizontal grids, as well as coupled land, sea ice, wave, marine biogeochemical, and river runoff models. The large ensemble consists of 100 ensemble members run from 1850 to 2100 and forced by CMIP6 historical (1850-2014) and SSP3-7.0 protocols (2015-2100) [13]. The SSP3-7.0 scenario, which has a high rate of emissions, was selected to investigate climate variability and its projected future changes. Anomalies were calculated by subtracting the ensemble mean from each ensemble member. We excluded SST data from our analysis at grid points where the ensemble-mean sea ice fraction exceeded 15% for any month during the time period considered.

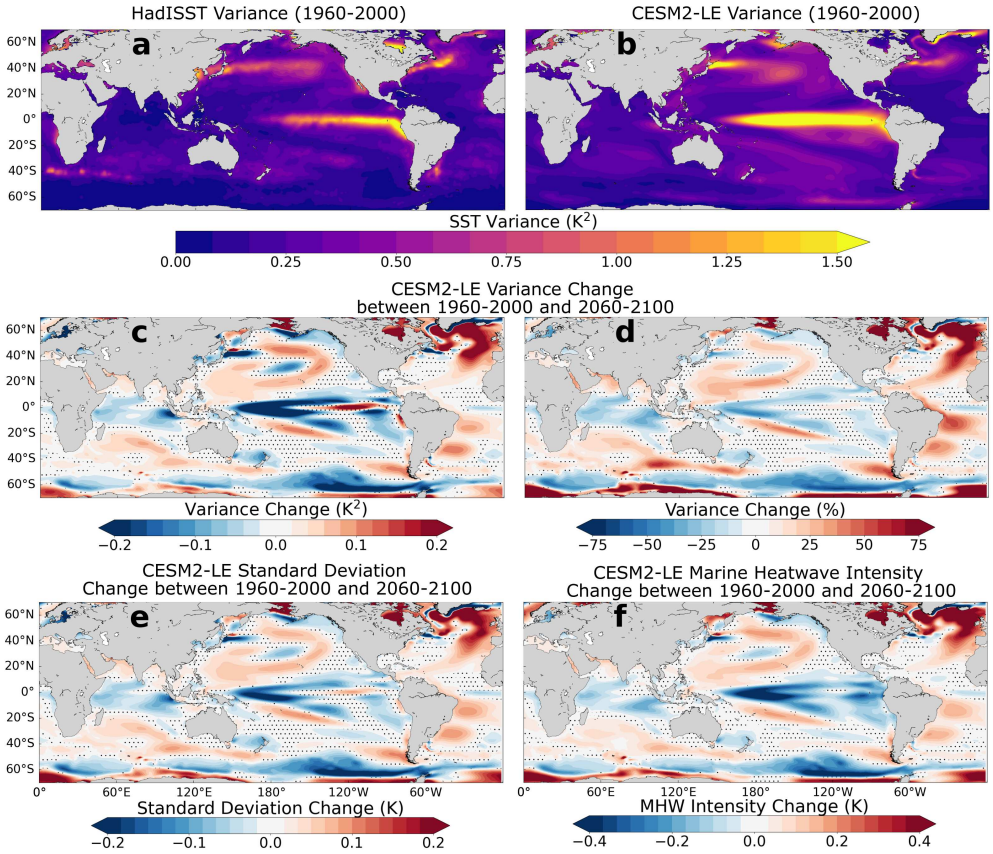

Fig. 1 (a) SST variance during 1960-2000 from HadISST and (b) from CESM2-LE. (c) SST variance change in CESM2-LE between 1960-2000 and 2060-2100. (d) Relative SST variance change between those time periods. (e) SST standard deviation change in CESM2-LE between 1960-2000 and 2060-2100. (f) Change of mean marine heatwave (MHW) intensity between 1960-2000 and 2060-2100. Stippled areas in (c)-(f) show where the change of the variance, standard deviation, or marine heatwave intensity is not significant at the 5% level.

Additionally we used several observational and reanalysis products to compare the CESM2-LE results in the historical period (1960-2000 unless otherwise noted). We used SSTs from the Hadley Centre Global Sea Ice and Sea Surface Temperature v1.1 dataset (HadISST [27]); sea level pressure and 850-hPa winds from the ECMWF Reanalysis v5 (ERA5 [28]); mixed layer depth from the Ocean Reanalysis System 5 (ORAS5 [29]), which is defined as the depth where the density exceeds the near surface density by 0.01 kg m^{-3}; turbulent surface heat fluxes from the 1° Objectively Analyzed air-sea Fluxes (OAFLUX [30]); and radiative surface heat fluxes from OAFLUX

(derived from the ISCCP-D product [31]) and Clouds and Earth's Radiant Energy Systems Energy Balanced and Filled Ed4.2 product (CERES EBAF [32]). Anomalies were calculated by subtracting the climatology for the entire time period used and then detrending with a linear fit. We excluded HadISST data from our analysis at grid points with sea ice cover (i.e., NaN values in the data) during any month from January 1960 to January 2000.

For the radiative heat fluxes, we calculated anomalies separately for OAFLUX (January 1985 to February 2000) and CERES EBAF (March 2000 to December 2022), and then combined the two sets of anomalies. We spatially smoothed this heat flux data using a moving average filter with 3-by-3-grid-cell window size. For computations requiring both heat flux and SST data, we also spatially smoothed the HadISST data in the same manner. Note that the CESM2-LE data was not smoothed.

2.2 Marine Heatwave Intensity

Marine heatwaves were defined using a 90^{th}-percentile threshold for monthly SST anomaly computed for each calendar month using all ensemble members [33]. The mean marine heatwave intensity at a given grid point was calculated as the mean SST anomaly of all 90^{th}-percentile exceedances over time and all ensemble members.

2.3 Linear Stochastic-Deterministic Model

To quantify the effect of different drivers on SST variance, we used an extension of the original local linear stochastic climate model [34, 35] with seasonally modulated feedback and noise forcing [36, 37] and an ENSO teleconnection term [38–40]. We use the formulation developed in refs. [41–43] that includes seasonal modulations in the feedback, noise forcing, and the ENSO teleconnection term:

$$\frac{\partial T'(t)}{\partial t} = \tilde{\lambda} T'(t) + \tilde{\beta} N(t) + \xi(t), \tag{1}$$

where T' is the SST anomaly at a given location, $\tilde{\lambda}$ is a seasonally modulated feedback coefficient, $\tilde{\beta}$ is a seasonally modulated ENSO teleconnection coefficient, N is the Niño3.4 index (the SST anomaly averaged over 5°N-5°S, 170°W-120°W), and ξ is stochastic forcing (i.e., "weather noise"). Averaged over the annual cycle, $\tilde{\lambda}$ must be negative so that SST anomalies are damped and do not grow without bound. $\tilde{\lambda}^{-1}$ has units of time and represents the decay timescale of SST anomalies, thus we refer to it hereafter to as the "ocean memory" [44].

The parameters $\tilde{\lambda}$ and $\tilde{\beta}$ are defined as

$$\tilde{\lambda} = \lambda_0 + \lambda_1 \sin(\omega_a t) + \lambda_2 \cos(\omega_a t), \tag{2}$$

$$\tilde{\beta} = \beta_0 + \beta_1 \sin(\omega_a t) + \beta_2 \cos(\omega_a t), \tag{3}$$

where ω_a is the angular frequency of the annual cycle ($2\pi/12$ months^{-1}) and λ_1, λ_2, β_1, and β_2 determine the amplitude and phase of the seasonal modulation. Physically, the seasonal modulation of these coefficients reflects seasonal changes of air-sea heat fluxes and the mixed layer heat capacity, the latter which is proportional to the mixed layer depth [41, 45]. For ease of display we present these coefficients as annual averages in this report (the amplitude and phase of $\tilde{\lambda}$ and $\tilde{\beta}$ are shown in Supplementary Fig. 1).

The noise term ξ primarily represents stochastic forcing from the atmosphere. It includes all processes that are uncorrelated with local SST anomalies and remote ENSO forcing, chiefly anomalous air-sea heat fluxes and anomalous Ekman advection of the SST gradient due to weather variability [46]. Entrainment and other ocean processes can also contribute to the forcing [47, 48]. ξ should be nearly white given the fast decorrelation timescale of the atmosphere [34, 49].

At each grid point for each ensemble member, equation 1 was fitted to the SST anomaly data using multiple linear regression (see ref, [42]). $\partial T'/\partial t$ was computed

using the forward finite difference method. The noise forcing ξ was taken to be the residual from the fit. This residual is well-described by white noise (see Supplementary Fig. 2), supporting the suitability of our choice of theoretical SST model.

2.4 SST Feedback Decomposition

The SST feedback coefficient $\tilde{\lambda}$ is the sum of several different atmospheric and oceanic feedbacks [48, 50–52]:

$$\tilde{\lambda} = \tilde{\lambda}_{\mathrm{SH}} + \tilde{\lambda}_{\mathrm{LH}} + \tilde{\lambda}_{\mathrm{SW}} + \tilde{\lambda}_{\mathrm{LW}} + \tilde{\lambda}_{\mathrm{ent}} + \tilde{\lambda}_{\mathrm{diff}} + \tilde{\lambda}_{\mathrm{other}} \tag{4}$$

where $\tilde{\lambda}_{\mathrm{SH}}$, $\tilde{\lambda}_{\mathrm{LH}}$, $\tilde{\lambda}_{\mathrm{SW}}$, $\tilde{\lambda}_{\mathrm{LW}}$ are the feedbacks associated with the sensible, latent, shortwave, and longwave components of the air-sea heat flux, respectively; $\tilde{\lambda}_{\mathrm{ent}}$ is the feedback due to entrainment as the mixed layer deepens in fall and winter; $\tilde{\lambda}_{\mathrm{diff}}$ is the feedback due to horizontal eddy diffusion, and $\tilde{\lambda}_{\mathrm{other}}$ is the feedback due to non-local and other processes not considered here.

We calculate the air-sea heat flux feedbacks given heat flux component x by fitting the following equation using multiple linear regression:

$$Q'_x(t) = \tilde{\lambda}^*_x T'(t) + \tilde{\beta}^*_x N(t) + \xi^*_x(t), \tag{5}$$

where $Q'_x(t)$ is the heat flux anomaly (defined as positive downward), $\tilde{\lambda}^*_x$ is the feedback for that heat flux component (with units $\mathrm{Wm^{-2}K^{-1}}$), and $\xi^*_x(t)$ is the noise forcing. $\tilde{\lambda}^*_x$ is related to the feedbacks $\tilde{\lambda}_x$ in equation 4 by the following:

$$\tilde{\lambda}_x = \frac{\tilde{\lambda}^*_x}{\rho c_p \tilde{H}} \tag{6}$$

where ρ is the density of seawater (1024 kg m^{-3}), c_p is the heat capacity of seawater (4001 J kg^{-1} K^{-1}), and $\tilde{H}$ is the monthly mixed layer depth climatology. To fit this equation to observations, we used the whole time period available for the heat flux data to minimize the error: January 1985 to December 2022 instead of the 1960-2000 period for fitting equation 1.

The feedback due to entrainment is

$$\tilde{\lambda}_{\text{ent}} = -\frac{\tilde{w}_{\text{ent}}}{\tilde{H}}\left(1 - \left\langle \frac{\partial T_b'}{\partial T'} \right\rangle\right), \tag{7}$$

where $\tilde{w}_{\text{ent}}$ is the entrainment velocity climatology, the time derivative of the mixed layer depth climatology $\tilde{H}$, and T_b' is the temperature below the mixed layer, with angled brackets denoting the ensemble/time mean (see ref. [50]). If T_b' is uncorrelated with T', and assuming a mixed layer of average depth 75 meters with an annual cycle amplitude of 100 meters, $\tilde{\lambda}_{\text{ent}} \approx -0.1$ months^{-1} when averaged over the annual cycle. Entrainment also leads to the phenomenon of "reemergence": often the SST anomaly from the previous winter persists under the mixed layer during summer and in fall is re-entrained into the mixed layer, leading to the reemergence of SST anomalies [53, 54]. Reemergence is not modeled in this work.

The feedback due to horizontal eddy diffusion is

$$\tilde{\lambda}_{\text{diff}} = \frac{\partial}{\partial T'}\left(\kappa \nabla^2 T'\right), \tag{8}$$

where κ is the horizontal eddy diffusivity. Assuming SST anomalies with a sinusoidal spatial structure of wavelength L, the feedback can be estimated via scaling analysis as

$$\tilde{\lambda}_{\text{diff}} \approx -\kappa \frac{4\pi^2}{L^2}. \tag{9}$$

For $L \approx 1000$ km (i.e., a length scale of ~ 160 km) and $\kappa \approx 500$ m^{2}s^{-1} (note that κ is a function of length scale and geographic location; see ref. [55]), $\lambda_{\text{diff}} \approx -0.05$ months^{-1}.

Equation 4 can be rewritten as

$$\tilde{\lambda} = \frac{\tilde{\lambda}^*_{\text{turb}}}{\rho c_p \tilde{H}} + \frac{\tilde{\lambda}^*_{\text{rad}}}{\rho c_p \tilde{H}} + \tilde{\lambda}_{\text{res}}, \tag{10}$$

where $\tilde{\lambda}^*_{\text{turb}}$ is the turbulent ($\tilde{\lambda}^*_{\text{SH}}$+$\tilde{\lambda}^*_{\text{LH}}$) heat flux feedback, $\tilde{\lambda}^*_{\text{rad}}$ is the radiative ($\tilde{\lambda}^*_{\text{SW}}$+$\tilde{\lambda}^*_{\text{LW}}$) heat flux feedback, and $\tilde{\lambda}_{\text{res}}$ is the residual feedback. $\tilde{\lambda}_{\text{res}}$ includes $\tilde{\lambda}_{\text{ent}}$, $\tilde{\lambda}_{\text{diff}}$, $\tilde{\lambda}_{\text{other}}$, and errors in estimating the air-sea feedbacks. From the estimations above, $\tilde{\lambda}_{\text{ent}}$+$\tilde{\lambda}_{\text{diff}} \approx -0.15$ months^{-1}, thus we expect $\tilde{\lambda}_{\text{res}}$ to have a similar value if there are not substantial errors in the calculation of the feedbacks and contributions from other unmodeled feedbacks. Because the large number of degrees of freedom in CESM2-LE (100 members) allows for robust statistical estimates of the atmospheric feedbacks, we expect $\tilde{\lambda}_{\text{res}}$ to primarily reflect damping by entrainment and diffusion. However, for observations/reanalysis, uncertainties in the heat flux, SST, and mixed layer depth data may compound to produce substantial errors in the calculated feedbacks and thus $\tilde{\lambda}_{\text{res}}$ may primarily reflect these errors rather than just damping from oceanic processes.

The change in the feedback can be expanded from equation 10 as

$$\Delta\tilde{\lambda} = \frac{\Delta\tilde{\lambda}^*_{\text{turb}}}{\rho c_p \tilde{H}_0} + \frac{\Delta\tilde{\lambda}^*_{\text{rad}}}{\rho c_p \tilde{H}_0} + \underbrace{\frac{-\tilde{\lambda}^*_{\text{turb},0} - \tilde{\lambda}^*_{\text{rad},0}}{\rho c_p \tilde{H}_0^2}\Delta\tilde{H}}_{\Delta\tilde{\lambda}_H} + \Delta\tilde{\lambda}_{\text{res}}, \tag{11}$$

where Δ indicates the change between the two time periods, a subscript 0 indicates that the value from the first time period is used and $\Delta\tilde{\lambda}_H$ is the change in the air-sea heat flux feedback due to the change in the mixed layer depth climatology.

2.5 Applicability of the Linear Stochastic-Deterministic Model

Equation 1 describes SSTs forced solely by the atmosphere: anomalous air-sea heat fluxes and anomalous Ekman advection of the mean SST gradient from stochastic weather processes and remote forcing from ENSO. Contributions to the variance from internal ocean dynamics (e.g., geostrophic advection, mixed layer depth variability, and entrainment) are neglected [56]. This simplification is inadequate to explain SST variance in the equatorial oceans, where coupled ocean-atmosphere dynamics in the Pacific give rise to ENSO; in western boundary currents, where ocean dynamics are important [57–59]; and in the areas of the North Atlantic and Southern Ocean where the thermohaline circulation contributes to SST variability on long timescales [60, 61].

In previous studies, the applicability of a linear stochastic model to SST dynamics was tested by goodness of fit to a theoretical power spectrum [50, 57], by establishing a threshold of sea surface height variance over which oceanic processes were assumed to dominate [62], or by comparing advection of SST anomalies with the estimated feedback term [45].

We used an objective criterion based on the lagged covariance of SST anomalies T' and net surface heat flux anomalies Q', R_{TQ} (see refs. [50, 56, 63]). If SST anomalies are both damped and forced by Q', at negative lags (when the ocean leads), R_{TQ} should be negative, corresponding to damping of SST anomalies by Q'. At positive lags (when the atmosphere leads), R_{TQ} should be positive, corresponding to forcing of SST anomalies by Q'. Thus we considered that any grid point which had $R_{TQ} < 0$ at negative lags (averaged over lags -3 to -1 months and all ensemble members) and $R_{TQ} > 0$ at positive lags (averaged over lags 1 to 3 months and all ensemble members) to be well represented by a linear stochastic model forced by the atmosphere. The grid points that did not meet this criterion were excluded from our analysis and are shown as white hashed areas in the Fig.s. As expected these grid points are in areas of high oceanic variability and strong air-sea coupling, such as the equatorial Pacific and

Kuroshio-Oyashio Extension region. For observations, as with the calculation of the air-sea heat flux feedbacks, this criteria was evaluated using data from January 1985 to December 2022. Supplementary Fig. 3 shows R_{TQ} at several representative locations.

2.6 Isolating SST Variance Contribution from Each Driver

Once $\tilde{\lambda}$, $\tilde{\beta}$, and ξ are determined, the SST variance due to changes in the corresponding drivers–the ocean memory, ENSO teleconnection, and noise forcing—can be isolated. We used two forward integrations, one isolating the SST anomalies forced only by the ENSO teleconnection T'_N and the other isolating SST anomalies forced only by noise T'_ξ:

$$T'_N(k+1) = T'_N(k) + \left[\tilde{\lambda}(m)T'_N(k) + \tilde{\beta}(m)N(k)\right]\Delta t, \tag{12}$$

$$T'_\xi(k+1) = T'_\xi(k) + \left[\tilde{\lambda}(m)T'_\xi(k) + \xi(k)\right]\Delta t, \tag{13}$$

where k is the time index, m is the month index (k mod 12), and Δt is the time step (one month). $\xi(k)$ was constructed using a shuffled fit residual (for each ensemble member): for each calendar month, the year was randomly shuffled, producing noise forcing that is temporally uncorrelated (i.e., white) but retains spatial correlations and seasonal variance modulation present in the fit residual. Our results differ little if the original fit residual (that contains both spatial correlations and a slight temporal autocorrelation) or a version in which the time dimension of the noise forcing is shuffled in a different random order at each grid point (and thus is white in both time and space; see Supplementary Fig. 4).

To isolate the change in variance due to the change of each driver, we performed six of these integrations with parameters from different time periods (see Tab. 1). Each integration was initialized with the SST anomaly at the beginning of the specified time period (2060-2100 for case C). We calculated the change in variance due to the

Table 1 Integration Parameters

$T'_{x,n}$	$\tilde{\lambda}$	$\tilde{\beta}$, $N(t)$	$\xi(t)$
$T'_{N,\mathrm{A}}$	1960-2000	1960-2000	-
$T'_{\xi,\mathrm{A}}$	1960-2000	-	1960-2000
$T'_{N,\mathrm{B}}$	2060-2100	2060-2100	-
$T'_{\xi,\mathrm{B}}$	2060-2100	-	2060-2100
$T'_{N,\mathrm{C}}$	1960-2100	2060-2100	-
$T'_{\xi,\mathrm{C}}$	1960-2100	-	2060-2100

change in each driver using the following expressions:

$$\Delta^{\lambda}\sigma^2(T') = \Big[\sigma^2\big(T'_{N,\mathrm{B}}\big) + \sigma^2\big(T'_{\xi,\mathrm{B}}\big)\Big] - \Big[\sigma^2\big(T'_{N,\mathrm{C}}\big) + \sigma^2\big(T'_{\xi,\mathrm{C}}\big)\Big], \tag{14}$$

$$\Delta^{N}\sigma^2(T') = \sigma^2\big(T'_{N,\mathrm{C}}\big) - \sigma^2\big(T'_{N,\mathrm{A}}\big), \tag{15}$$

$$\Delta^{\xi}\sigma^2(T') = \sigma^2\big(T'_{\xi,\mathrm{C}}\big) - \sigma^2\big(T'_{\xi,\mathrm{A}}\big), \tag{16}$$

where $\Delta^{x}\sigma^2(T')$ is the change in SST variance due to changes to the driver x, $\sigma^2(T'_{x,n})$ is the variance of the integrated SST time series corresponding to the case letter n (A, B, or C) in Tab. 1.

2.7 Statistical Significance Testing

All parameters shown in this report (e.g., $\sigma^2(T'_{x,n})$, $\tilde{\lambda}$, $\tilde{\beta}$) were calculated for each ensemble member, creating 100 independent samples. Welch's t-test was then used to assess the statistical significance of ensemble-mean changes of these parameters between 1960-2000 and 2060-2100 [64]. Except in areas with minimal changes, the null hypothesis of no change between the two time periods is rejected at the 5% level.

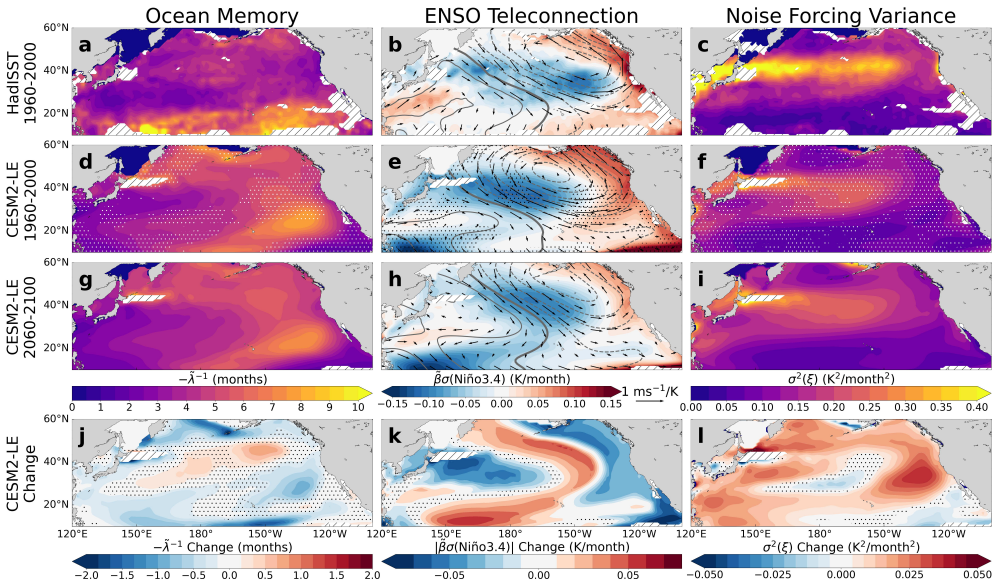

Fig. 2 Equation 1 parameters fit to HadISST (a)-(c) and CESM2-LE (d)-(i) SST data in shaded contours, with CESM2-LE projected changes on the bottom row (j)-(l). (b), (e), (h) vectors and contours are the 850-hPa winds and sea level pressure regressed onto the Niño3.4 index, the latter with 0.25-hPa/K spacing (positive values are solid lines and negative lines are dashed, with a thicker line at the zero contour). Stippling in (d)-(f) indicates that the parameters derived from observations lie outside the 5$^{\text{th}}$-95$^{\text{th}}$ percentile range of those derived from the CESM2-LE ensemble members. Stippling in (j)-(l) indicates where the changes are not significant at the 5% level. The ocean memory and ENSO teleconnection panels show the mean over the seasonal cycle, and all CESM2-LE panels are the ensemble mean. Locations where the SST data is not well-described by a local linear stochastic model are shown as white hatched areas (see Section 2.5).

3 Results & Discussion

3.1 Ocean Memory and Its Future Changes

The ocean memory varies considerably across the North Pacific, both in observations and CESM2. Over most of the North Pacific, the ocean memory diagnosed from the observations is between 2-6 months (Fig. 2a). Equatorward of about 20°N, particularly toward the eastern side the basin, the ocean memory is substantially longer, typically around 9 months. The magnitude of the ocean memory is largely consistent with previous estimations (e.g., refs. [40, 56]) and the autocorrelation timescale of large-scale modes such as the the Pacific Decadal Oscillation [39].

In the observations, the contribution of the different heat fluxes to the total feedback (Fig. 3a-c) shows strong damping from turbulent heat fluxes (almost entirely the latent heat feedback) particularly in a band at 25°N in the western North Pacific. Over much of the North Pacific poleward of 20°N, the radiative heat flux feedback (almost entirely shortwave feedback) is positive, indicative of the low cloud-SST feedback, where negative SST anomalies are associated with increased atmospheric stability, leading to the formation of low clouds which reduce surface shortwave radiation and further cool the ocean [65–67].

The ocean memory in CESM2-LE is similar in magnitude to observations, ranging between about 2 and 9 months, but has a distinct spatial pattern (Fig. 2d, g). The ocean memory is shorter in the western North Pacific than in the east, which can mostly be attributed to strong damping by turbulent heat fluxes (Fig. 3d). As in the observations, the turbulent and radiative feedbacks are dominated by the latent heat and shortwave feedbacks, respectively (see Supplementary Fig. 5). A large area of particularly long ocean memory is present between Hawai‘i and North America, resulting from relatively weak turbulent heat flux damping and positive radiative feedback, likely from the low cloud-SST feedback.

Interestingly, the phases of $\tilde{\lambda}$ and $\tilde{H}$ differ: $\tilde{\lambda}$ is most strongly negative between August and December (depending on location) whereas $\tilde{H}$ is deepest between December and March (see Supplementary Fig. 1). That implies that the seasonality of the air-sea heat flux feedbacks play a strong role in the seasonal modulation of $\tilde{\lambda}$ in addition to that of the mixed layer depth.

In observations, the residual feedback has considerable spatial structure (Fig. 3c), with areas of negative and strongly positive feedbacks. In CESM2-LE, the residual feedback is negative everywhere except for coastal areas off China and Mexico. As related in Section 2.3, entrainment and horizontal eddy diffusion are expected to damp

SST anomalies, with a combined feedback on the order of -0.15 months^{-1}, which corresponds well with the results from CESM2-LE. However, the strong positive feedbacks in observations could be the result of errors in the heat flux and mixed layer depth data. The magnitude of the feedbacks $\tilde{\lambda}_x^*$ for different heat flux components are similar between observations and CESM2-LE (see Supplementary Fig. 5). However, the mixed layer depth is typically somewhat deeper in CESM2-LE than in the ORAS5 reanalysis, which would lead to the $\tilde{\lambda}_{\text{rad}}$ and $\tilde{\lambda}_{\text{turb}}$ being greater in magnitude in observations compared to CESM2-LE. Part of that discrepancy may be due to the different mixed layer definitions used: a density-based definition for ORAS5 (see Section 2.1) and a buoyancy-based definition for CESM2 [68].

In the future climate in CESM2-LE, the ocean memory declines over most of the basin except for a zonally-elongated area in the central North Pacific where it increases (Fig. 2j). The changes to the individual feedbacks are are spatially varied, but it appears that the change in ocean memory is primarily driven by changes to the radiative and residual feedbacks, suggesting that changes in clouds and ocean dynamics are most important for the change in ocean memory. In common with other climate models (e.g., refs. [44, 69]), the mixed layer depth in the North Pacific in CESM2-LE is shallower nearly everywhere in the future climate, leading to a reduced heat capacity and correspondingly shorter ocean memory (Fig. 3g). However, the magnitude of the feedback change due to the shallower mixed layer is relatively minor compared to the changes to the other feedbacks, in contrast with the findings of ref. [44], who attributed the projected decline in ocean memory in CMIP6 models primarily to mixed layer depth shallowing.

3.2 ENSO Teleconnection and Its Future Changes

The ENSO teleconnection, represented by $\tilde{\beta}$ multiplied by the standard deviation of Niño3.4, in both observations and CESM2-LE (Fig. 2b, e, h) exhibits the well-known

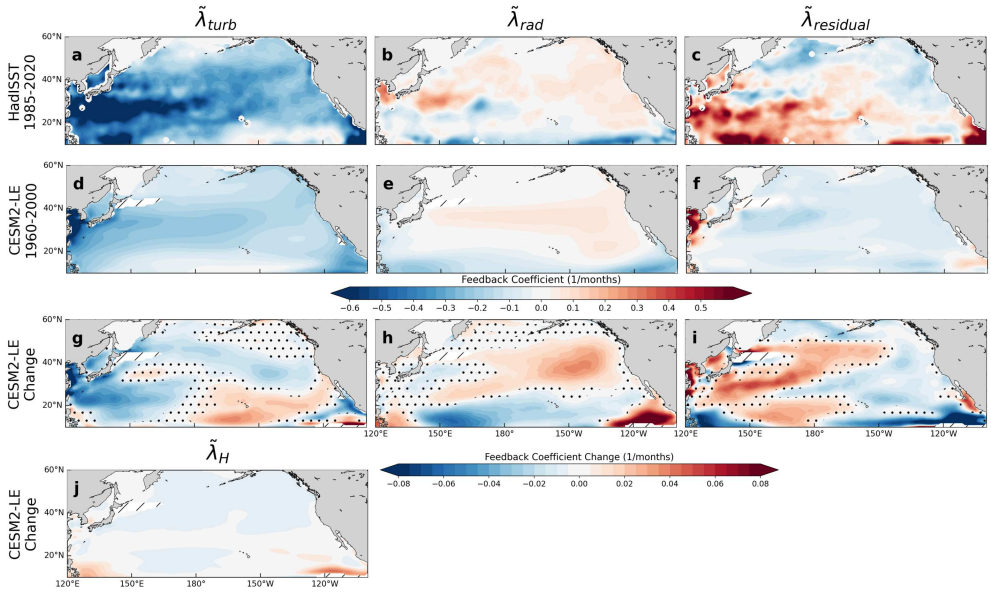

Fig. 3 (a)-(f) Turbulent, radiative, and residual SST feedbacks in HadISST and CESM2-LE for 1960-2000. (g)-(i) Changes to those feedbacks in CESM2-LE between 1960-2000 and 2060-2100, with (j) showing the contribution of the mixed layer depth change. Stippling in (g)-(i) indicates where the changes are not significant at the 5% level. All panels show the feedbacks averaged over the seasonal cycle and the CESM2-LE panels showing the ensemble mean. Locations where the SST data does not meet the criterion described in Section 2.5 are shown as white hatched areas.

"atmospheric bridge" pattern: cooling of SSTs in the central North Pacific and warming in the eastern North Pacific during El Niño (and the reverse during La Niña) [70–72]. This pattern is caused by anomalous tropical heating in the central Pacific during El Niño which excites atmospheric Rossby wave trains that propagate poleward and induce changes in atmospheric circulation and surface heat fluxes. The Aleutian Low deepens during El Niño, resulting in anomalous cold and dry northwesterly winds over the central North Pacific that cool SSTs and anomalous warm and humid southeasterly winds over the eastern North Pacific that warm SSTs. These changes in wind, air temperature, and humidity modulate the air-sea heat fluxes, resulting in SST anomalies. These large-scale atmospheric patterns are evident in the sea level pressure and 850-hPa wind regressed onto the Niño3.4 index (line contours and vectors in Fig. 2b, e, h).

The spatial pattern of the teleconnection in CESM2-LE for 1960-2000 is broadly similar to the observed pattern but is displaced slightly to the west and is somewhat stronger in magnitude. The westward displacement likely is due to the ENSO SST anomaly in CESM2 extending further west than in observations [73]. However, in most of the North Pacific the observed teleconnection falls within two cross-ensemble standard deviations. At the center of action in the central North Pacific, the annually-averaged teleconnection coefficient $\tilde{\beta}$ is much stronger in observations than in CESM2-LE for either time period (see Supplementary Fig. 6). However, the ensemble mean Niño3.4 standard deviation in CESM2-LE is about 50% greater than in observations: 1.30 K and 1.26 K for 1960-2000 and 2060-2100, respectively, compared to the observed value of 0.86 K for 1960-2000 in HadISST. Thus, the overall magnitude of forcing of the teleconnection on SST anomalies is comparable between the model and observations.

In CESM2-LE, the ENSO teleconnection pattern shifts to the northeast in the future climate. The teleconnection, both in its effect on atmospheric circulation and SSTs, weakens slightly. That shift likely is caused by the eastward shift of the location of maximum precipitation during ENSO due to the expansion of the western Pacific warm pool (see refs. [74, 75]). Changes to the atmospheric waveguide may also contribute to the teleconnection shift.

3.3 Noise Forcing and Its Future Changes

The variance of the noise forcing ξ has a broad maximum at 40°N in both the observations and CESM2-LE, stretching from Japan to about 150°W (Fig. 2c, f, i). This coincides with the subarctic SST front and the North Pacific storm track, thus high atmospheric and oceanic variability in this region is expected. The noise in observations has considerably greater variance than in CESM2-LE even though the SST variance is similar. Because SST variance increases with increasing ocean memory

(in an AR-1 process; see ref. [76]), the greater noise variance in observations is compensated by the somewhat shorter ocean memory to yield comparable overall SST variance to CESM2-LE.

The future change of the noise forcing variance is spatially heterogeneous in CESM2-LE. Although increasing in most areas, particularly in the eastern North Pacific between Hawai'i and North America, there are areas in the central and southeastern parts of the basin where noise variance decreases. The strong increase in variance north of Japan is potentially due to a poleward shift of the Kuroshio [77].

3.4 Drivers of future SST Variance Change

As described in Section 2.6 we used the fitted values of $\tilde{\lambda}$, $\tilde{\beta}$, and ξ to create several sets of reconstituted SST data forced either by ENSO or by the noise residual ξ. The variance of the ENSO-forced SSTs is appreciably smaller than the noise-forced SSTs (Fig. 4b-c). However, the *change* in variance of the ENSO-forced SSTs due to the shift of the ENSO teleconnection is comparable in magnitude to the change in variance of the noise-forced SSTs (Fig. 4e-f). The sum of the individual variance changes sums to close to the true variance change, supporting the validity of integrating the forcings separately (compare Fig. 4a and g).

The pattern of variance change due to each of the three drivers closely resembles the changes to the corresponding parameters in Fig. 2j-i. Increases in the ocean memory lead to increased SST variance and vice versa, as expected for an AR-1 process (see ref. [76]). Likewise, increases in the magnitude of the ENSO teleconnection and noise forcing lead to increases in SST variance, and vice versa. The change in the strength of the ENSO teleconnection is almost entirely a function of the change in $\tilde{\beta}$ as the change in the Niño3.4 variance is small between the two time periods in CESM2-LE.

Fig. 4h shows the contribution of each driver to the overall variance change by assigning the change due to each driver to a color channel (red=$\Delta^{\xi}\sigma^2(T')$,

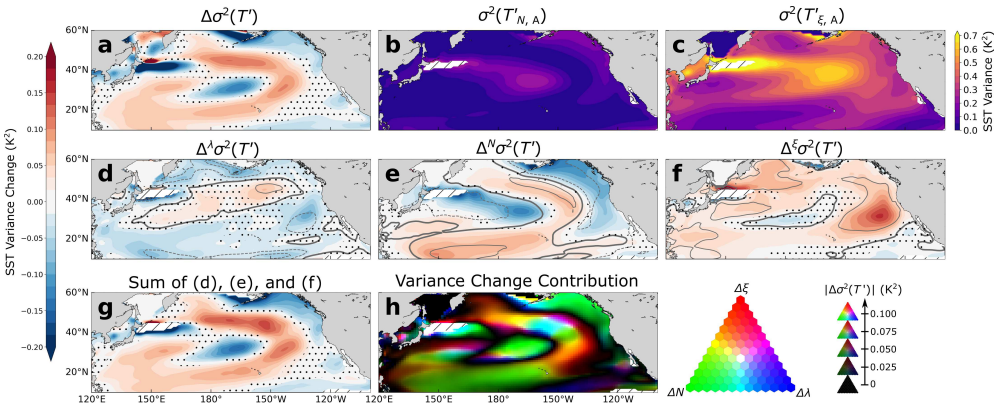

Fig. 4 (a) The total SST variance change as in Fig. 1c. (b) and (c) The SST variance associated with ENSO-only and noise-only forcing, respectively, for 1960-2000. (d)-(f) The SST variance changes associated with the change in ocean memory, the ENSO teleconnection, and stochastic noise. The grey contours represent the same changes as in Fig. 2j-l: the change of the ocean memory $\tilde{\lambda}^{-1}$, ENSO teleconnection $\tilde{\beta}\sigma$(Niño3.4), and the noise variance $\sigma(\xi)$, respectively. The zero contour line is thicker, with contour intervals of 0.67 months, 0.04 K/month, and 0.02 K/month, respectively. (g) The total SST variance change computed by summing (d), (e), and (f). (h) The contribution of the change of each driver to the SST variance change. Hue indicates the relative contribution of each driver and brightness corresponds to the magnitude of the total SST variance change (see Supplementary Fig. 7). Locations where the SST data does not meet the criterion described in Section 2.5 are shown as white hatched areas. Stippling indicates where the changes are not significant at the 5% level.

green=$\Delta^N\sigma^2(T')$, blue=$\Delta^\lambda\sigma^2(T')$). At each grid point, a driver was only considered to contribute to the change in variance if its associated variance change was of the same sign as the total SST variance change (i.e., if at some grid point $\Delta\sigma^2(T') > 0$ and $\Delta^\lambda\sigma^2(T') < 0$, the change in $\tilde{\lambda}$ was considered to not contribute to the overall change in variance). Then the variance of the drivers that do contribute to the SST variance change is represented by a mix of colors, with the hue signifying the relative contribution of each driver, and the brightness being proportional to the magnitude of the total SST variance change. The construction of this visualization is detailed in Supplementary Fig. 7.

As evidenced by the large areas of green in Fig. 4h, the shift of the ENSO teleconnection dominates the SST variance change pattern. The arcuate pattern in the central North Pacific and the decrease in variance in the Gulf of Alaska are almost entirely due to the shift in the teleconnection. The change in the stochastic noise forcing contributes to a lesser extent, with its greatest influence being northeast of

Hawai'i. In most of the North Pacific, decreased SST variance due to declining ocean memory is compensated for by increased variance due to increasing stochastic noise forcing. That memory is generally declining and noise increasing implies that the "damped-persistence" predictability of SST anomalies will decline in the future in most areas.

We also assessed the contribution of the change of each driver by using the pattern correlation, defined as the Pearson correlation coefficient between two arrays weighted by the cosine of the latitude. Areas of the arrays where the R_{TQ} criterion described in Section 2.5 are not met were removed. In the North Pacific (10°N-60°N, 120°E-100°W) the pattern correlations between the total variance change (as in Fig. 4g) and the variance changes due to individual drivers are 0.15 for $\Delta^{\lambda}\sigma^2(T')$, 0.76 for $\Delta^{N}\sigma^2(T')$, and 0.47 for $\Delta^{\xi}\sigma^2(T')$. Those correlations support the above conclusion that the shift in the ENSO teleconnection is most important to the overall change in SST variance, followed by the change in the stochastic noise, with the change in ocean memory playing only a minor role.

4 Conclusions

In this work, we have demonstrated a conceptual model of SST variability that can explain the drivers behind future change of projected SST variance. By using this framework, we were able to quantify the SST variance change between 1960-2000 and 2060-2100 to three drivers:

- *Ocean Memory* – The ocean memory declines over most of the North Pacific with an elongated region in the center of the basin exhibiting longer memory in the future. We attribute this change primarily to changes in air-sea feedbacks and ocean damping, the latter presumably due to changes in horizontal diffusion and entrainment. The latent heat and shortwave feedbacks, the latter likely due to the low cloud-SST feedback, are the most important air-sea feedbacks. The shallowing mixed layer

depth appears to play a secondary role. The change in ocean memory plays a minor role in the overall change in SST variance as its impact is largely compensated for by increases in stochastic noise forcing.

- *ENSO Teleconnections* – The "atmospheric bridge," which connects North Pacific SSTs to ENSO events via atmospheric Rossby waves, shifts to the northeast in the future climate. Although the extratropical SST variance associated with remote ENSO forcing is much smaller than the variance driven by stochastic noise, the shift of the ENSO teleconnection pattern results in a large change in SST variance, dominating the overall change in SST variance.
- *Stochastic Noise Forcing* – The noise forcing, computed as a residual from a fit to an extended local linear stochastic-deterministic model (equation 1), increases in most of the North Pacific. Its impact on SST variance is somewhat attenuated by the change in the ocean memory.

These findings have implications for predictability – the generally lower ocean memory and higher noise forcing suggests that predictability of a simple "damped persistence" model will decline in skill in the future climate in most regions. ENSO is a major source of SST predictability on seasonal timescales, hence the shift of its teleconnections results in ENSO-associated changes in predictability in different regions. Our results highlight the importance of studies into future ENSO changes and its regional impacts.

Although this study was focused narrowly on the North Pacific and the CESM2-LE model, our framework should be equally applicable to other extratropical oceans and other climate models. Different large ensemble climate models show considerable diversity in their future ENSO dynamics [5], thus contribution of the various drivers of SST variability may differ greatly between models. This study also did not determine the physical mechanisms responsible for the change in ocean memory and stochastic

noise forcing and how they relate to climate mean state changes. We aim to answer these questions in future work.

Acknowledgements

This study was supported by NOAA's Climate Program Office's Modeling, Analysis, Predictions, and Projections (MAPP) program under grant NA20OAR4310445 and NSF grant AGS-2141728. JLG acknowledges the support of the Uehiro Center for the Advancement of Oceanography. MFS participates in the MAPP Marine Ecosystem Task Force. The authors acknowledge helpful discussions with Fei-Fei Jin, Niklas Schneider, and Brian Powell. The CESM2-LE simulations were conducted on the Aleph supercomputer through a partnership between the Institute for Basic Sciences (IBS) Center for Climate Physics (ICCP) in South Korea and the CESM group at the National Center for Atmospheric Research (NCAR) in the U.S., representing a broad collaborative effort between scientists from both centers. Special thanks goes to Axel Timmermann, Keith Rodgers, Sun-Seon Lee, Nan Rosenbloom, and Jim Edwards from those institutions. This is IPRC publication X and SOEST contribution Y.

Author Contributions

JLG and MFS conceived of the methodology in this report. JLG analyzed the data and wrote the draft manuscript. SZ was a major contributor to the coding behind the analysis. All authors have read and approved the final manuscript.

Competing Interests

The authors have no competing interests to declare.

Data Availability

The CESM2-LE data are available via the Earth System Grid (https://www.earthsystemgrid.org), the HadISST data are available from the Met Office (https://www.metoffice.gov.uk/hadobs/hadisst/), the ERA5 and ORAS5 data are available via the Climate Data Store (https://cds.climate.copernicus.eu), the OAFLUX data are available from WHOI (https://oaflux.whoi.edu/), and the CERES data are available from NASA (https://ceres.larc.nasa.gov/).

Code Availability

The code and data required to reproduce the figures is available via Zenodo (https://doi.org/10.5281/zenodo.10419764).

References

1. Manabe, S. & Wetherald, R. T. Thermal Equilibrium of the Atmosphere with a Given Distribution of Relative Humidity. *Journal of the Atmospheric Sciences* **24,** 241–259 (1967).
2. Cai, W. *et al.* Increased variability of eastern Pacific El Niño under greenhouse warming. *Nature* **564,** 201–206 (2018).
3. Cai, W. *et al.* in *Geophysical Monograph Series* (eds McPhaden, M. J., Santoso, A. & Cai, W.) 1st ed., 289–307 (Wiley, 2020).
4. Geng, T. *et al.* Emergence of changing Central-Pacific and Eastern-Pacific El Niño-Southern Oscillation in a warming climate. *Nature Communications* **13,** 6616 (2022).
5. Maher, N. *et al.* The future of the El Niño–Southern Oscillation: using large ensembles to illuminate time-varying responses and inter-model differences. *Earth System Dynamics* **14,** 413–431 (2023).

6. Wengel, C. *et al.* Future high-resolution El Niño/Southern Oscillation dynamics. *Nature Climate Change* **11,** 758–765 (2021).

7. Timmermann, A. *et al.* Increased El Niño frequency in a climate model forced by future greenhouse warming. *Nature* **398** (1999).

8. Ying, J. *et al.* Emergence of climate change in the tropical Pacific. *Nature Climate Change* **12,** 356–364 (2022).

9. Bui, H. X. & Maloney, E. D. Changes in Madden-Julian Oscillation Precipitation and Wind Variance Under Global Warming. *Geophysical Research Letters* **45,** 7148–7155 (2018).

10. Bui, H. X. & Maloney, E. D. Changes to the Madden-Julian Oscillation in Coupled and Uncoupled Aquaplanet Simulations With 4xCO_2. *Journal of Advances in Modeling Earth Systems* **12** (2020).

11. Jenney, A. M., Randall, D. A. & Barnes, E. A. Drivers of uncertainty in future projections of Madden–Julian Oscillation teleconnections. *Weather and Climate Dynamics* **2,** 653–673 (2021).

12. Rushley, S. S., Kim, D. & Adames, Á. F. Changes in the MJO under Greenhouse Gas–Induced Warming in CMIP5 Models. *Journal of Climate* **32,** 803–821 (2019).

13. Rodgers, K. B. *et al.* Ubiquity of human-induced changes in climate variability. *Earth System Dynamics* **12,** 1393–1411 (2021).

14. Stouffer, R. J. & Wetherald, R. T. Changes of Variability in Response to Increasing Greenhouse Gases. Part I: Temperature. *Journal of Climate* **20,** 5455–5467 (2007).

15. Van der Wiel, K. & Bintanja, R. Contribution of climatic changes in mean and variability to monthly temperature and precipitation extremes. *Communications Earth & Environment* **2,** 1 (2021).

16. Deser, C. *et al.* Insights from Earth system model initial-condition large ensembles and future prospects. *Nature Climate Change* **10,** 277–286 (2020).

17. Li, W. *et al.* Future changes in the frequency of extreme droughts over China based on two large ensemble simulations. *Journal of Climate* **34,** 6023–6035 (2021).

18. Maher, N. *et al.* The Max Planck Institute Grand Ensemble: Enabling the Exploration of Climate System Variability. *Journal of Advances in Modeling Earth Systems* **11,** 2050–2069 (2019).

19. Hawkins, E. & Sutton, R. The Potential to Narrow Uncertainty in Regional Climate Predictions. *Bulletin of the American Meteorological Society* **90,** 1095–1108 (2009).

20. Deser, C., Alexander, M. A., Xie, S.-P. & Phillips, A. S. Sea Surface Temperature Variability: Patterns and Mechanisms. *Annual Review of Marine Science* **2,** 115–143 (2010).

21. Smith, K. E. *et al.* Biological Impacts of Marine Heatwaves. *Annual Review of Marine Science* **15,** 119–145 (2023).

22. Smith, K. E. *et al.* Socioeconomic impacts of marine heatwaves: Global issues and opportunities. *Science* **374,** eabj3593 (2021).

23. Oliver, E. C. *et al.* Marine Heatwaves. *Annual Review of Marine Science* **13,** 313–342 (2021).

24. Amaya, D. J. *et al.* Marine heatwaves need clear definitions so coastal communities can adapt. *Nature* **616,** 29–32 (2023).

25. Jacox, M. G., Alexander, M. A., Bograd, S. J. & Scott, J. D. Thermal displacement by marine heatwaves. *Nature* **584,** 82–86 (2020).

26. Danabasoglu, G. *et al.* The Community Earth System Model Version 2 (CESM2). *Journal of Advances in Modeling Earth Systems* **12** (2020).

548 27. Rayner, N. A. Global analyses of sea surface temperature, sea ice, and night
549 marine air temperature since the late nineteenth century. *Journal of Geophysical*
550 *Research* **108,** 4407 (2003).
551 28. Hersbach, H. *et al.* The ERA5 global reanalysis. *Quarterly Journal of the Royal*
552 *Meteorological Society* **146,** 1999–2049 (2020).
553 29. Zuo, H., Balmaseda, M. A., Tietsche, S., Mogensen, K. & Mayer, M. The
554 ECMWF operational ensemble reanalysis–analysis system for ocean and sea ice:
555 a description of the system and assessment. *Ocean Science* **15,** 779–808 (2019).
556 30. Yu, L. & Weller, R. A. Objectively Analyzed Air–Sea Heat Fluxes for the Global
557 Ice-Free Oceans (1981–2005). *Bulletin of the American Meteorological Society*
558 **88,** 527–540 (2007).
559 31. Rossow, W. B. & Schiffer, R. A. Advances in Understanding Clouds from ISCCP.
560 *Bulletin of the American Meteorological Society* **80,** 2261–2288 (1999).
561 32. Kato, S. *et al.* Surface Irradiances of Edition 4.0 Clouds and the Earth's Radiant
562 Energy System (CERES) Energy Balanced and Filled (EBAF) Data Product.
563 *Journal of Climate* **31,** 4501–4527 (2018).
564 33. Deser, C. *et al.* Future changes in the Intensity and Duration of Marine Heat and
565 Cold Waves: Insights from Coupled Model Initial-Condition Large Ensembles.
566 *Journal of Climate* (2024).
567 34. Hasselmann, K. Stochastic climate models. Part I: Theory. *Tellus* **28,** 473–485
568 (1976).
569 35. Frankignoul, C. & Hasselmann, K. Stochastic climate models. Part II: Applica-
570 tion to sea-surface temperature anomalies and thermocline variability. *Tellus* **29,**
571 289–305 (1977).
572 36. De Elvira, A. R. & Lemke, P. A Langevin equation for stochastic climate models
573 with periodic feedback and forcing variance. *Tellus* **34,** 313–320 (1982).

37. Nicholls, N. The Southern Oscillation and Indonesian Sea Surface Temperature. *Monthly Weather Review* **112,** 424–432 (1984).

38. Newman, M., Compo, G. P. & Alexander, M. A. ENSO-Forced Variability of the Pacific Decadal Oscillation. *Journal of Climate* **16,** 3853–3857 (2003).

39. Newman, M. *et al.* The Pacific Decadal Oscillation, Revisited. *Journal of Climate* **29,** 4399–4427 (2016).

40. Schneider, N. & Cornuelle, B. D. The Forcing of the Pacific Decadal Oscillation. *Journal of Climate* **18,** 4355–4373 (2005).

41. Stuecker, M. F. *et al.* Revisiting ENSO/Indian Ocean Dipole phase relationships. *Geophysical Research Letters* **44,** 2481–2492 (2017).

42. Zhao, S., Jin, F.-F. & Stuecker, M. F. Improved Predictability of the Indian Ocean Dipole Using Seasonally Modulated ENSO Forcing Forecasts. *Geophysical Research Letters* **46,** 9980–9990 (2019).

43. Stuecker, M. F. The climate variability trio: stochastic fluctuations, El Niño, and the seasonal cycle. *Geoscience Letters* **10,** 51 (2023).

44. Shi, H. *et al.* Global decline in ocean memory over the 21st century. *Science Advances* **8,** eabm3468 (2022).

45. Frankignoul, C., Kestenare, E. & Mignot, J. The surface heat flux feedback. Part II: direct and indirect estimates in the ECHAM4/OPA8 coupled GCM. *Climate Dynamics* **19,** 649–655 (2002).

46. Larson, S. M., Vimont, D. J., Clement, A. C. & Kirtman, B. P. How Momentum Coupling Affects SST Variance and Large-Scale Pacific Climate Variability in CESM. *Journal of Climate* **31,** 2927–2944 (2018).

47. Alexander, M. A. & Penland, C. Variability in a Mixed Layer Ocean Model Driven by Stochastic Atmospheric Forcing. *Journal of Climate* **9,** 2424–2442 (1996).

48. Patrizio, C. R. & Thompson, D. W. J. Understanding the Role of Ocean Dynamics in Midlatitude Sea Surface Temperature Variability Using a Simple Stochastic Climate Model. *Journal of Climate* **35,** 3313–3333 (2022).

49. Lorenz, E. N. Deterministic Nonperiodic Flow. *Journal of the Atmospheric Sciences* **20,** 130–141 (1963).

50. Frankignoul, C. Sea surface temperature anomalies, planetary waves, and air-sea feedback in the middle latitudes. *Reviews of Geophysics* **23,** 357 (1985).

51. Haney, R. L. Surface Thermal Boundary Condition for Ocean Circulation Models. *Journal of Physical Oceanography* **1,** 241–248 (1971).

52. Patrizio, C. R. & Thompson, D. W. J. Quantifying the Role of Ocean Dynamics in Ocean Mixed Layer Temperature Variability. *Journal of Climate* **34,** 2567–2589 (2021).

53. Alexander, M. A. & Deser, C. A Mechanism for the Recurrence of Wintertime Midlatitude SST Anomalies. *Journal of Physical Oceanography* **25,** 122–137 (1995).

54. Deser, C., Alexander, M. A. & Timlin, M. S. Understanding the Persistence of Sea Surface Temperature Anomalies in Midlatitudes. *Journal of Climate* **16,** 57–72 (2003).

55. Nummelin, A., Busecke, J. J. M., Haine, T. W. N. & Abernathey, R. P. Diagnosing the Scale- and Space-Dependent Horizontal Eddy Diffusivity at the Global Surface Ocean. *Journal of Physical Oceanography* **51,** 279–297 (2021).

56. Frankignoul, C. & Reynolds, R. W. Testing a Dynamical Model for Mid-Latitude Sea Surface Temperature Anomalies. *Journal of Physical Oceanography* **13,** 1131–1145 (1983).

57. Reynolds, R. W. Sea surface temperature anomalies in the North Pacific Ocean. *Tellus* **30,** 97–103 (1978).

625 58. Schneider, N. & Miller, A. J. Predicting Western North Pacific Ocean Climate.
626 *Journal of Climate* **14,** 3997–4002 (2001).
627 59. Qiu, B. The Kuroshio Extension System: Its Large-Scale Variability and Role
628 in the Midlatitude Ocean-Atmosphere Interaction. *Journal of Oceanography* **58,**
629 57–75 (2002).
630 60. Delworth, T. L. & Greatbatch, R. J. Multidecadal Thermohaline Circulation
631 Variability Driven by Atmospheric Surface Flux Forcing. *Journal of Climate* **13,**
632 1481–1495 (2000).
633 61. Zhang, R. *et al.* A Review of the Role of the Atlantic Meridional Overturning
634 Circulation in Atlantic Multidecadal Variability and Associated Climate Impacts.
635 *Reviews of Geophysics* **57,** 316–375 (2019).
636 62. Hall, A. & Manabe, S. Can local linear stochastic theory explain sea surface
637 temperature and salinity variability? *Climate Dynamics* **13,** 167–180 (1997).
638 63. Frankignoul, C. & Kestenare, E. The surface heat flux feedback. Part I: estimates
639 from observations in the Atlantic and the North Pacific. *Climate Dynamics* **19,**
640 633–647 (2002).
641 64. Welch, B. L. The Generalization of 'Student's' Problem when Several Different
642 Population Variances are Involved. *Biometrika* **34,** 28 (1947).
643 65. Norris, J. R. & Leovy, C. B. interannual Variability in Stratiform Cloudiness and
644 Sea Surface Temperature. *Journal of Climate* **7,** 1915–1925 (1994).
645 66. Clement, A. C., Burgman, R. & Norris, J. R. Observational and Model Evidence
646 for Positive Low-Level Cloud Feedback. *Science* **325,** 460–464 (2009).
647 67. Xie, S.-P. *Coupled Atmosphere-Ocean Dynamics: From El Niño to Climate*
648 *Change* (Elsevier, Amsterdam, 2023).
649 68. Large, W. G., Danabasoglu, G., Doney, S. C. & McWilliams, J. C. Sensitivity to
650 Surface Forcing and Boundary Layer Mixing in a Global Ocean Model: Annual-
651 Mean Climatology. *Journal of Physical Oceanography* **27,** 2418–2447 (1997).

69. Capotondi, A., Alexander, M. A., Bond, N. A., Curchitser, E. N. & Scott, J. D. Enhanced upper ocean stratification with climate change in the CMIP3 models. *Journal of Geophysical Research: Oceans* **117** (2012).

70. Alexander, M. A. *et al.* The Atmospheric Bridge: The Influence of ENSO Teleconnections on Air–Sea Interaction over the Global Oceans. *Journal of Climate* **15,** 2205–2231 (2002).

71. Lau, N.-C. & Nath, M. J. The Role of the "Atmospheric Bridge" in Linking Tropical Pacific ENSO Events to Extratropical SST Anomalies. *Journal of Climate* **9,** 2037–2057 (1996).

72. Taschetto, A. S. *et al.* in *El Niño southern oscillation in a changing climate* First Edition, 311–335 (Wiley-American Geophysical Union, Hoboken, NJ, 2020).

73. Chen, H.-C., Fei-Fei-Jin, Zhao, S., Wittenberg, A. T. & Xie, S. ENSO Dynamics in the E3SM-1-0, CESM2, and GFDL-CM4 Climate Models. *Journal of Climate* **34,** 9365–9384 (2021).

74. Power, S., Delage, F., Chung, C., Kociuba, G. & Keay, K. Robust twenty-first-century projections of El Niño and related precipitation variability. *Nature* **502,** 541–545 (2013).

75. Yan, Z. *et al.* Eastward shift and extension of ENSO-induced tropical precipitation anomalies under global warming. *Science Advances* **6,** eaax4177 (2020).

76. Von Storch, H. & Zwiers, F. W. *Statistical Analysis in Climate Research* (Cambridge University Press, Cambridge, 1999).

77. Yang, H. *et al.* Intensification and poleward shift of subtropical western boundary currents in a warming climate. *Journal of Geophysical Research: Oceans* **121,** 4928–4945 (2016).

677 78. Welch, P. The use of fast Fourier transform for the estimation of power spectra:
678 A method based on time averaging over short, modified periodograms. *IEEE*
679 *Transactions on Audio and Electroacoustics* **15,** 70–73 (1967).

Supplementary Files

This is a list of supplementary files associated with this preprint. Click to download.

- SupplementaryInformation.pdf